ISSN 1064-2269, Journal of Communications Technology and Electronics, 2018, Vol. 63, No. 3, pp. 270–276. © Pleiades Publishing, Inc., 2018.
Original Russian Text © A.T. Gazizov, A.M. Zabolotskii, T.R. Gazizov, 2018, published in Radiotekhnika i Elektronika, 2018, Vol. 63, No. 3, pp. 292–298.

NOVEL RADIO SYSTEMS AND ELEMENTS

Measurement and Simulation of Time Response of Printed Modal Filters with Broad-Side Coupling

A. T. Gazizov*, A. M. Zabolotskii, and T. R. Gazizov*****

Tomsk State University of Control Systems and Radio Electronics, Tomsk, 634050 Russia

**e-mail: alexandr.bbm@gmail.com*

***e-mail: zabolotsky_am@mail.ru*

****e-mail: talgat@tu.tusur.ru*

Received April 2, 2016

Abstract—A principle of modal filtering and an asymmetric modal filter with broad-side coupling are presented. Prototypes with different parameters are developed and fabricated. Experimental measurements and computer simulation are performed for the time response to a pulse with a duration of about 1 ns. It is shown that the simulated results are in agreement with the experimental data. Attenuation of the input pulse by a factor of 5 is demonstrated for the modal filter with optimal parameters for a 50-Ω circuit.

DOI: 10.1134/S1064226918030087

INTRODUCTION

There has been considerable recent interest in the protection of critical radio electronic equipment (REE) against intentional electromagnetic interference [1–3]. Special attention is paid to high-power nanosecond and subnanosecond pulses, since such pulses can penetrate in REE being slightly attenuated in conventional protection systems [4–7]. Modal filters (MFs) can be as promising protecting devices that represent passive structures capable of suppressing ultrashort pulses (USPs) due to splitting into pulses with smaller amplitudes owing to the difference of delays of signal propagation modes in a coupled line with inhomogeneous dielectric filling [8]. Relatively small mass, high reliability, and radiation stability are significant advantages of MFs. Cable MFs have been developed and fabricated for applications in power-supply circuits [9, 10], and printed MFs have been designed for the Fast Ethernet network [11]. The time response of a new printed MF (asymmetric MF with broad-side coupling that is characterized by relatively simple structure, significant attenuation, and substantial difference of the mode delays) to a trapezoid input pulse has been numerically simulated in [12–15].

The purpose of this paper is to experimentally study the USP propagation in an asymmetric MF with broad-side coupling at different parameters of the transverse cross section and compare experimental results and the results of simulation with exact imitation of the shape of the real signal.

1. MODAL FILTER WITH BROAD-SIDE COUPLING

The modal filtering is based on the application of modal distortions (modifications of signal related to the difference of the mode delays of transverse waves in a multiconductor transmission line) for the protection. A pulse that is excited in an active conductor of a fragment of dielectric-filled line consisting of N_{cond} conductors (except for the reference one) may exhibit modal distortions upon propagation (including splitting into N_{cond} pulses with smaller amplitudes) owing to the difference of the mode delays per unit length in the line [16]. A pulse is completely decomposed under the following condition:

$$t_\Sigma < l\min|\tau_{i+1} - \tau_i|, \quad i = 1, ..., N_{cond} - 1, \qquad (1)$$

where t_Σ is the total pulse duration at the zero level, l is the length of the fragment, and τ_i is the delay per unit length for the ith mode of the fragment. For $N_{cond} = 2$, condition (1) is reduced to

$$t_\Sigma < l|\tau_e - \tau_o| \qquad (2)$$

where τ_e and τ_o are the delays per unit length for even and odd modes in the fragment of coupled lines.

When a pulse with duration shorter than the difference of mode delays is fed to a fragment of a pair of coupled conductors between any of them and the reference conductor, two pulses can be obtained at the end of the fragment between the same conductors. Note that the pulse amplitudes at the end of the fragment are two times less than the pulse amplitude at the beginning of the fragment. Stronger electromagnetic coupling of the line conductors causes a decrease in the amplitudes of the pulses resulting from splitting. In particular, the attenuation coefficient of the printed MF with broad-side (strong) coupling (Fig. 1a) is greater than the attenuation coefficient for a structure with edge (weak) coupling (Fig. 1b) by a factor of 3.5 [17]. Note also that the maximum duration of the splitted pulse for the system of Fig. 1a is greater than

the maximum duration for the system of Fig. 1b by a factor of 10. With respect to the frequency response function, the MF represents a low-pass filter, and the pass band for the desired signal can be controlled through MF parameters.

We consider the transverse cross section of the MF with broad-side coupling (Fig. 1a): active (A), reference (R) and passive (P) parallel conductors are located on the substrate with thickness h and permittivity ε_r. The input signal is fed between the active and reference conductors. The presence of the passive conductor that is strongly coupled with the active conductor leads to the splitting of the input signal into the output signals of the even and odd modes. The conductor width is w, the conductor thickness is t, the distance between the conductors is s, and the distance between the end of the structure and the conductor is d.

Figure 2 presents the MF connection circuit: e is the emf source, R_1 and R_3 are the resistances of the source and load, R_2 and R_4 are the MF resistances, and U is the node of the MF output voltage. The scheme shows the ends of the active and passive conductors (A and P, respectively), and the symbol of grounding is used to show the reference conductor.

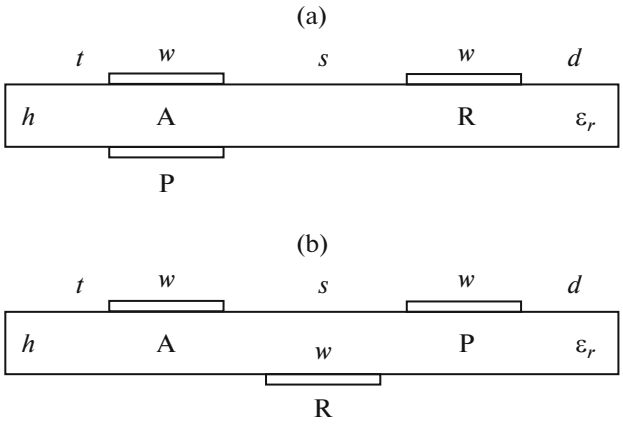

Fig. 1. Transverse cross sections of MFs with (a) broad-side and (b) edge coupling.

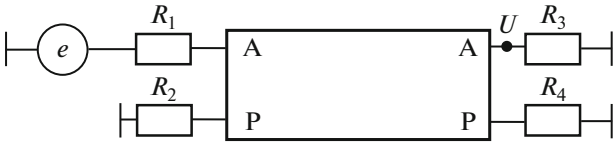

Fig. 2. MF connection circuit.

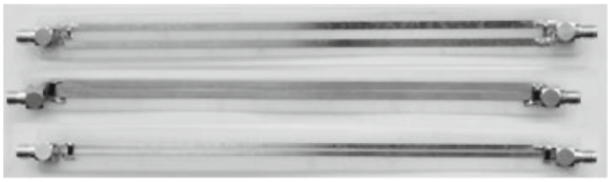

Fig. 3. Photograph of the MF prototypes.

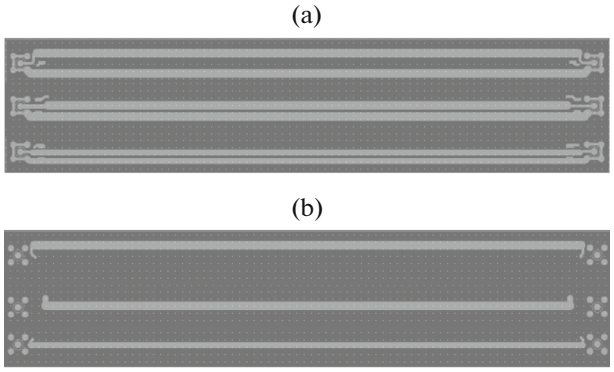

Fig. 4. Photomasks of (a) A and (b) B sides of the MF board.

2. PROTOTYPE DEVELOPMENT AND FABRICATION

The interval of the geometrical parameters of the MF prototypes is chosen with respect to requirements on minimization, economic expediency, and maximum transmitted current. Two-side foil-clad fiberglass plate with the parameters $h = 0.18$ mm and $t = 65$ μm is chosen due to cheapness and common availability. The TALGAT [18] computer simulation using genetic algorithms is used to determine optimal (with respect to maximum difference of the mode delays per unit length) parameters: $s = 3$ mm and $w = d = 4$ mm for the MF in the 50-Ω circuit. MF resistances of $R_2 = R_4 = 50\ \Omega$ are chosen to minimize the reflections. Additional prototypes are used to roughly estimate the sensitivity of the time response to deviations from the optimal parameters. The length of each prototype is 0.2 m. The SMA connectors are soldered to the inputs and outputs of each prototype for connection to the measurement devices. For convenience, we use serial numbers for the prototypes with the following parameters: $w = 3$ mm and $s = 4$ mm (MF prototype 1), $w = 3$ mm and $s = 1$ mm (MF prototype 2), and $w = 2$ mm and $s = 1$ mm (MF prototype 3). Figures 3 and 4 show the photographs and photomasks of the prototypes.

3. SIMULATION AND MEASUREMENT PROCEDURES

3.1. Simulation Procedure

For the simulation of the time response, we employ quasi-static analysis based on fast and accurate mathematical models in the TALGAT system, which allows analysis of regular transmission lines with arbitrary cross sections. A fragment of the transmission line with N_{cond} signal conductors and one reference conductor is described for the given transverse cross section using the following matrices of the parameters per

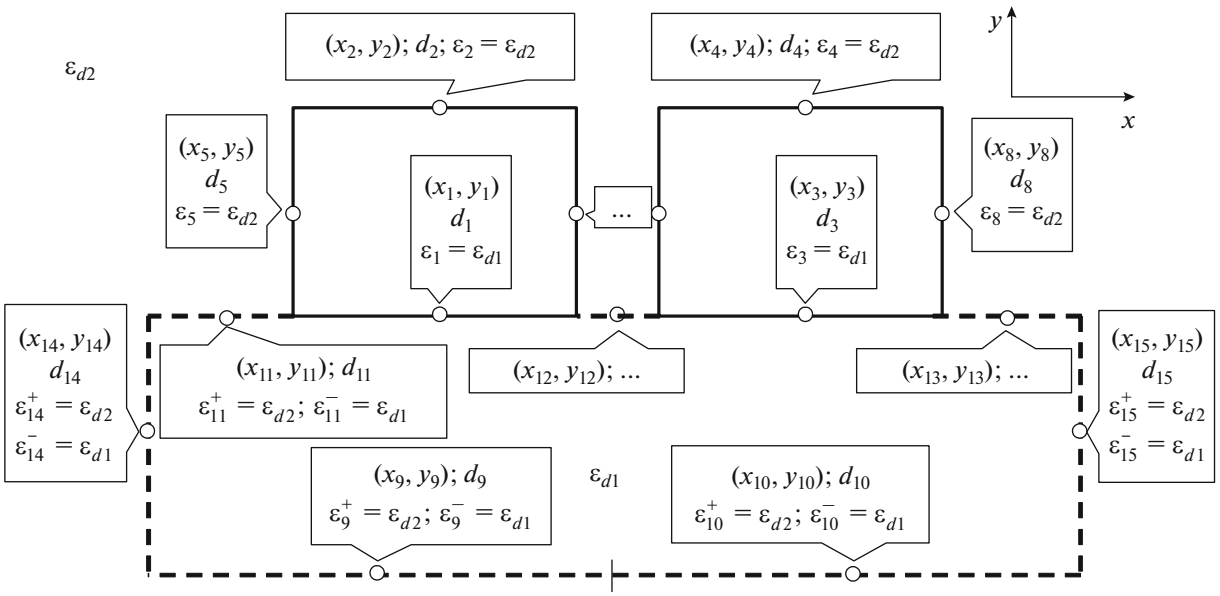

Fig. 5. 2D configuration with (solid lines) conductor–dielectric and (dashed lines) dielectric–dielectric boundaries.

unit length: electrostatic induction **C**, inductance **L**, resistance **R**, and conductance **G**. The **L**, **C**, and **G** matrices are calculated with the aid of the method of moments [19]. The losses in conductors and dielectric are determined using matrices **R** and **G** with allowance for the frequency dependences of the matrices. Elements of matrix **R** are calculated with allowance for the skin effect. In the simulation, we assume that the parameters of substrate are frequency-independent and equal to the parameters at a frequency of 1 GHz ($\varepsilon_r = 4.5$ and $\tan\delta = 0.025$). For such parameters, we calculate matrix **G** and perform recalculation for different frequencies.

Periodic (in time domain) external signal is used, and the FFT for such a signal is performed. The method of modified node matrix of [20] is used to determine the voltage at the given node for each frequency. The time-domain voltage is obtained with the aid of the inverse Fourier transform.

3.2. Calculation of the Matrix of Coefficients of Electrostatic Induction

A mathematical model for the calculation of the matrix of coefficients of electrostatic induction has been proposed in [21] for the 2D configuration of conductors and dielectrics with linear boundaries oriented perpendicularly to the x and y axes of the Cartesian coordinates and the general scenario with arbitrary reference conductor (finite or as a plane). Such a model is characterized by simplicity of analytical expressions for the entries of matrix of the linear algebraic systems to solution of which the calculations are reduced. We use such a model for the finite reference conductor typical for the MF under study. Figure 5 shows an illustrating configuration: transverse cross section of a regular transmission line with two conductors on a dielectric substrate and the principle of segmentation.

First, we perform segmentation (division into fragments (subintervals)) for the conductor–dielectric boundaries and use numbers from 1 to N_c for the subintervals. First, the segmentation and numbering are performed for the subintervals that are orthogonal to the y axis (N_{cy} is the number of the last subinterval). Then, the same procedure is used for the subintervals that are orthogonal to the x axis (N_c is the last number). After that, the segmentation is performed for the dielectric–dielectric boundaries and numbers from $N_c + 1$ to N are used for the subintervals. The segmentation and numbering are sequentially performed for the subintervals that are orthogonal to the y and x axes (the last numbers are N_{dy} and N, respectively).

Each subinterval is described using the following parameters: x_n, coordinate of the x center of the nth subinterval; y_n, coordinate of the y center of the nth subinterval; d_n, length of the nth subinterval; ε_n, permittivity in the vicinity of the nth conductor–dielectric subinterval; and ε_n^+ and ε_n^-, permittivities on the positive (to which vector $\mathbf{n}_n$ is directed) and negative (from which vector $\mathbf{n}_n$ is directed) sides of the nth dielectric–dielectric subinterval (vector $\mathbf{n}_n$ is the unit vector that is orthogonal to the nth interval at its center). The parameters are used to calculate the entries of linear system matrix with the aid of the below formulas.

For lines with numbers $m = 1, ..., N_c$, we have

$$S_{mn} = -\frac{I_{mn}}{2\pi\varepsilon_0}, \quad \begin{cases} m = 1, \ldots, N_c \\ n = 1, \ldots, N \end{cases} \tag{1}$$

where ε_0 is the electric constant and

$$I_{mn} = a_1 \ln\left(a_1^2 + c_1^2\right) - 2a_1 + 2c_1 \arctan\left(\frac{a_1}{c_1}\right) - a_2 \ln\left(a_2^2 + c_2^2\right) + 2a_2 - 2c_1 \arctan\left(\frac{a_2}{c_1}\right).$$

Here, the coefficients for $n = 1, ..., N_{cy}, (N_c + 1), ..., N_{dy}$ are given by

$$a_1 = \frac{d_n}{2} - (x_m - x_n), \quad a_2 = \frac{-d_n}{2} - (x_m - x_n), \quad c_1 = y_m - y_n. \tag{2}$$

For $n = (N_{cy} + 1), ..., N_c, (N_{dy} + 1), ..., N$, the coefficients are written as

$$a_1 = \frac{d_n}{2} - (y_m - y_n), \quad a_2 = \frac{-d_n}{2} - (y_m - y_n), \quad c_1 = x_m - x_n. \tag{3}$$

For the lines with numbers $m = (N_c + 1), ..., N$, we have

$$S_{mn} = \frac{I_{mn}}{2\pi\varepsilon_0}, \quad \begin{cases} m = (N_c + 1), \ldots, N \\ n = 1, \ldots, N \end{cases}, \ m \neq n;$$

$$S_{mm} = \frac{I_{mm}}{2\pi\varepsilon_0} + \frac{1}{2\varepsilon_0}\frac{\varepsilon_m^+ + \varepsilon_m^-}{\varepsilon_m^+ - \varepsilon_m^-}, \quad m = (N_c + 1), \ldots, N,$$

where the following expression is valid for lines with numbers $m = (N_c + 1), ..., N_{dy}$ for $n = 1, ..., N_{cY}, (N_c + 1), ..., N_{dy}$:

$$I_{mn} = \arctan\left(\frac{a_1}{c_1}\right) - \arctan\left(\frac{a_2}{c_1}\right) \tag{4}$$

and variables coincide with those of expression (2) and the following expression is valid for $n = (N_{cy} + 1), ..., N_c, (N_{dy} + 1), ..., N$:

$$I_{mn} = \frac{1}{2}\ln\left(\frac{a_2^2 + c_1^2}{a_1^2 + c_1^2}\right) \tag{5}$$

where the variables coincide with those of expression (3). For the lines with numbers $m = (N_{dy} + 1), ..., N$ when $n = 1, ..., N_{cY}, (N_c + 1), ..., N_{dy}$, quantities I_{mn} are calculated using expression (5) with variables (2). For $n = (N_{cy} + 1), ..., N_c, (N_{dy} + 1), ..., N$, quantity I_{mn} is calculated with the aid of expression (4) where variables coincide with those of expression (3).

For the system under study in which the $(N_{\text{cond}} + 1)$th conductor is grounded, we follow the approach of [22] and add the $(N + 1)$th line and column with the elements

$$S_{nN+1} = \frac{d_n}{2S_{nn}}, \quad S_{N+1n} = d_n\varepsilon_n, \quad n = 1, \ldots, N_c.$$

Then, we form linear system

$$\sum_{n=1}^{N} S_{mn}\sigma_n = \begin{cases} V_i, & m = 1, \ldots, N_c, \\ 0, & m = (N_c + 1), \ldots, N. \end{cases}$$

Here subscript i is used to show that each discretization element of the ith conductor has a potential that is needed to determine the matrix of coefficients of electrostatic induction. Elements S_{mn} form square matrix $\mathbf{S}$ that establishes relationship of charge densities of discretization elements on conductors and dielectric boundaries that form vector $\boldsymbol{\sigma}$ and potential of these elements that form vector $\mathbf{V}$. Thus, the problem is represented as linear system $\mathbf{S}\boldsymbol{\sigma} = \mathbf{V}$ that is solved N_{cond} times in such a way that potential of conductor V_i ($i = 1, ..., N_{\text{cond}}$) is 1 V in the ith solution and 0 V for the remaining conductors. Finally, we have the following expression for an entry of the capacitance matrix:

$$C_{ij} = \sum_{n=NF_i}^{NL_i} \frac{\varepsilon_n}{\varepsilon_0}\sigma_n^{(j)} d_n, \quad i, j = 1, \ldots, N_{\text{cond}}.$$

Here, NF_i and NL_i are the numbers of the first and last subintervals of the ith conductor, i is the number of the conductor on which charges $\sigma_n^{(j)}$ are summed up, and j is the superscript for quantities σ_n that are calculated at potentials of 1 V for the jth conductor and 0 V for the remaining conductors.

3.3. Measurement Method

The time response is measured using an S9-11 computerized oscilloscope that represents a combination of a broadband stroboscopic oscilloscope, generator of the nano- and picosecond measurement signals, and built-in microcomputer. The input pulse (Fig. 6a) has an amplitude of 600 mV at a load of 50 Ω and a duration of 820 ps at a level of 0.1. For simulation, such a signal is digitized and used as the input signal in the TALGAT system (Fig. 6b).

4. SIMULATED AND EXPERIMENTAL RESULTS

Figure 7 shows the experimental and simulated time responses for the prototypes. Table 1 presents quantitative data.

5. DISCUSSION

We consider the results for each prototype. MF prototype 1 exhibits optimal parameters and provides

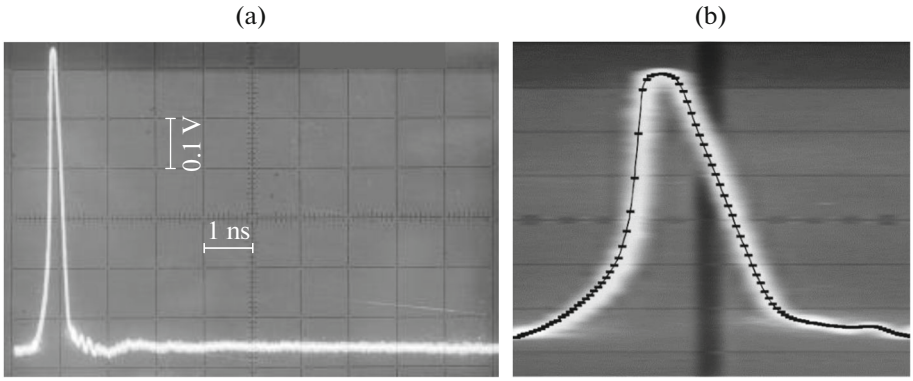

Fig. 6. (a) Input pulse and (b) horizontally expanded pulse shape with 10-ps markers.

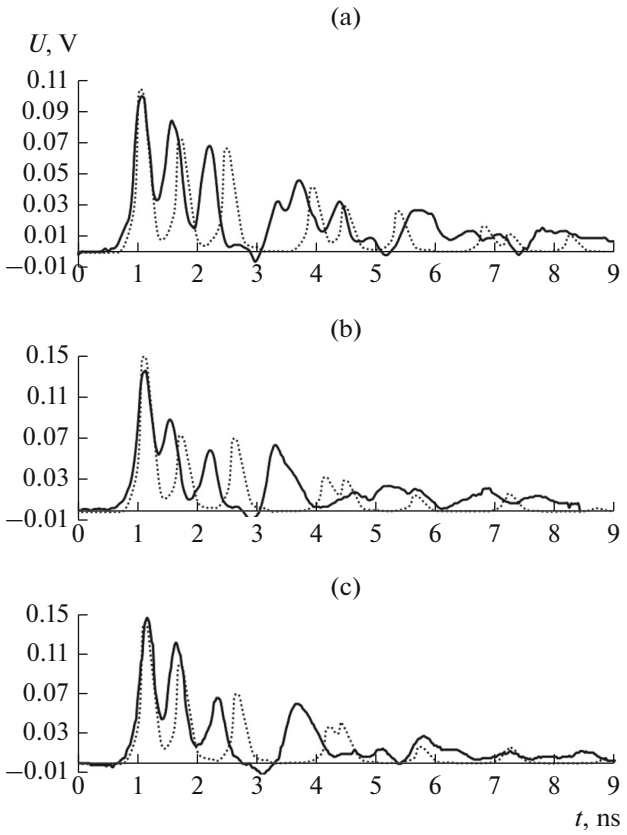

Fig. 7. (Solid lines) Experimental and (dotted lines) simulated time responses for MF prototypes (a) 1, (b) 2, and (c) 3.

attenuation of the input pulse by a factor of about 5. Figure 7a shows that the output signal represents a pulse train, in which the first pulse is the pulse of the even mode, the second pulse is the pulse of the odd mode, and the remaining pulses are the reflections of these pulses from the ends of the lines that arrive at 3, 5, ... line delays. Thus, we prove the modal splitting that makes it possible to decrease the amplitude of the output signal. MF prototype 2 has a smaller distance between the active and reference conductors in comparison with prototype 1, and the width of conductors of prototype 3 is less than the width of prototype 2. It is seen that the modal splitting takes place but the attenuation becomes worse by a factor of about 1.5. Such a result can be due to weaker coupling of the active and passive conductors, which results in an increase in the output amplitude.

The results of Fig. 7 and Table 1 show that the simulated output pulse amplitudes and differences of signal modes are less and greater, respectively, than the

Table 1. Quantitative comparison of simulated (S) and experimental (Exp) results ($\Delta = |(X_S - X_{Exp})/(X_S + X_{Exp})| \times 100\%$

Prototype no.	Peak voltage of the pulse, mV						Difference of delays for peak voltages, ns		
	first			second					
	S	Exp	Δ, %	S	Exp	Δ, %	S	Exp	Δ, %
1	100	113	6.1	65	90	16.1	0.72	0.6	9.1
2	143	145	0.7	72	95	13.8	0.67	0.6	5.5
3	145	153	2.7	97	120	10.6	0.69	0.6	7.0

corresponding measured parameters. For the time responses of Fig. 7, the noncoincidence of the differences of the delays per unit length is manifested as a delay of the simulated time response relative to the experimental response. Such a delay can be caused by incorrect permittivity ε_r of the substrate that is used in the simulation. A smaller value of the real permittivity accounts for the smaller difference of the pulse delays in the experiment and the consequent overlapping of the trailing edge of the first pulse and the leading edge of the second pulse, which results in an increase of the amplitude of the second pulse. Thus, we obtain a greater difference of the experimental and simulated voltages of the second pulse in comparison with the difference for the first pulse (see Table 1). The simulated results differ from the experimental results due to the fact that real sizes of MF differ from the sizes that are used in the simulation. In addition, note that the simulation is performed with disregard of the effect of (i) inhomogeneities introduced by the SMA connectors and their sites at the input and output of the MF and (ii) parasitic parameters, via, and sites of resistors. We also take into account a permissible measurement error of 7.5% of the S9-11 oscilloscope. Thus, we conclude that the simulated results are in agreement with the experimental data and the possible reasons for differences are determined.

CONCLUSIONS

We have experimentally studied the time response of an asymmetric MF with broad-side coupling to a pulse with a duration of about 1 ns and performed simulation with exact imitation of the real pulse shape. The results of the simulation with the real pulse shape are in agreement with the experimental results. However, the comparison of the results indicates that parameters of real dielectric must be used in the simulation. An attenuation factor of 5 is obtained for the maximum coupling and the optimal parameters of the MF in the 50-Ω circuit. We assume that the attenuation factor can be increased owing to equalization of the pulse amplitudes of the even and odd modes in more accurate simulation taking into account real loss in conductors and dielectric.

ACKNOWLEDGMENTS

The simulation was supported by the Ministry of Education and Science of the Russian Federation (project no. 8.9562.2017/8.9) and the experimental work was supported by the Russian Science Foundation (project no. 14-19-01232).

REFERENCES

1. *GOST R 52863-2007: Protected Automated Systems. Tests for Stability Against Intentional Electromagnetic Action* (Standartinform, Moscow, 2007).
2. N. Mora, F. Vega, G. Lugrin, et al., System and Design Assessment Notes, Note 41 (2014).
3. *GOST R 56103-2014: Protected Automated Systems. Organization and Structure of Activities for Protection Against Intentional Electromagnetic Action* (Standartinform, Moscow, 2014).
4. R. M. Gizatullin and Z. M. Gizatullin, *Noise Immunity and Information Security of Computer Systems Under Electromagnetic Action via Power Supply* (Kazan. Gos. Tekhn. Univ., Kazan, 2014).
5. T. R. Gazizov, A. M. Zabolotsky, A. O. Melkozerov et al., in *Proc. Eur. Electromagn. Symp. EUROEM-2012, Toulouse, France, July 2–6, 2012* (ONERA, Toulouse, 2012), p. 106.
6. K. Yu. Sakharov, A. A. Sokolov, O. V. Mikheev, et al. Tekhnol. EMS, No. 3(18), 36 (2006).
7. T. Weber, R. Krzikalla, and L. Haseborg, IEEE Trans. Electromagn. Compat. **46**, 297 (2004).
8. A. M. Zabolotskii and T. R. Gazizov. *Modal Filters for Protection of the Onboard Radio Electronic Equipment of Spacecraft* (Tomsk. Gos. Univ. Sist. Upravl. Radioelektron. (TUSUR), Tomsk, 2013).
9. T. R. Gazizov and A. M. Zabolotsky, IEEE Trans. Electromagn. Compat. **54**, 229 (2012).
10. T. R. Gazizov, A. M. Zabolotsky, and I. E. Samotin, in *Proc. Int. Siberian Conf. on Control and Communications (SIBCON–2009), Tomsk, Mar. 27–28, 2009*, p. 264.
11. T. R. Gazizov, I. E. Samotin, A. M. Zabolotsky, and A. O. Melkozerov, in *Proc. 30th Int. Conf. on Lightning*

Protection (ICLP), Cagliary, Sept. 13–17, 2010 (IEEE, New York, 2010).

12. A. M. Zabolotsky and A. T. Gazizov, Int. J. Circuits, Syst. Signal Processing **9**, 68 (2015).
13. A. T. Gazizov and A. M. Zabolotsky, in *Proc. 2015 Int. Siberian Conf. on Control and Communications (SIBCON), Omsk, May 21–23, 2015* (IEEE, New York, 2015), p. 7147024.
14. A. T. Gazizov, A. M. Zabolotsky, and O. A. Gazizova, in *Proc. 16th Int. Conf. of Young Specialists on Micro/Nanotechnologies and ElectronDevices (EDM 2015), Erlagol, 29 June–02 July, 2010* (IEEE, New York, 2010).
15. A. T. Gazizov, in *Proc. Asia Electromagn. Conf. (ASIAEM), Jeju Island, South Korea, Aug. 2–7, 2015* (Ihna Univ., 2015), p. 232.
16. T. R. Gazizov and A. M. Zabolotskii, Tekhnol. EMS, No. 4, 40 (2006).
17. A. T. Gazizov, in *Modern Problems of Radio Electronics* (Sib. Fed. Univ., Krasnoyarsk, 2015), p. 317. http://efir.sfu-kras.ru/wp-content/uploads/download/Сборник_СПР-2015.pdf.
18. S. P. Kuksenko, A. M. Zabolotskii, A. O. Melkozerov, T. R. Gazizov, Dokl. Tomsk. Gos. Univ., Sist. Upravl. Radioelektron., No. 2, 45 (2015).
19. A. R. Djordjevich, T. K. Sarkar, and R. F. Harrington, Proc. IEEE **75**, 743 (1987).
20. T. R. Gazizov, *Rec. 2001 IEEE Int. Symp. Electromagnetic Compability, Montreal, Aug. 13–17, 2001* (IEEE, New York, 2001), Vol. 1, p. 151.
21. J. R. Griffith and M. S. Nakhla, IEEE Trans. Microwave Theory Tech. **38**, 1480 (1990).
22. T. R. Gazizov, Izv. Vyssh. Uchebn. Zaved., Fiz. **47**, (3), 88 (2004).
23. M. R. Scheinfein and O. A. Palusinski, Trans. Soc. Comp. Simulat. Int. **4** (3), 187 (1987).

Translated by A. Chikishev